Check for updates

High-Resolution Capillary Printing of Eutectic Gallium Alloys for Printed Electronics

Navid Hussain, Tongtong Fu, Gabriel Marques, Chittaranjan Das, Torsten Scherer, Uwe Bog, Lukas Berner, Irene Wacker, Rasmus R. Schröder, Jasmin Aghassi-Hagmann,* and Michael Hirtz*

A versatile liquid metal (LM) printing process enabling the fabrication of various fully printed devices such as intra- and interconnect wires, resistors, diodes, transistors, and basic circuit elements such as inverters which are process compatible with other digital printing and thin film structuring methods for integration is presented. For this, a glass capillary-based direct-write method for printing LMs such as eutectic gallium alloys, exploring the potential for fully printed LM-enabled devices is demonstrated. Examples for successful device fabrication include resistors, p–n diodes, and field effect transistors. The device functionality and easiness of one integrated fabrication flow shows that the potential of LM printing is far exceeding the use of interconnecting conventional electronic devices in printed electronics.

1. Introduction

In the era of printed electronics (PE), low melting point metal alloys also called liquid metals (LMs) have become a focus of attraction because they exhibit as high electrical and thermal conductivity as many of the conventional metals or alloys, but simultaneously LMs are ductile and fluid at or near room temperature (RT), being processable by printing. Other advantages include the ability to withstand bending and being stretchable without losing their electrical conductivity and on deformation being fully reversible and fatigue-proof.[1–5] In contrast to the

use of metal precursors, metal powders, or metal nanoparticles based approaches, LMs do not require additional processing steps such as chemical reduction, or sintering, usually involving high temperature, intense light or vacuum processing which can be detrimental for many substrates used in PE. Over the past century, LMs have seen a dramatic increase in use for applications in PE, stretchable electronics, wearable electronics, or soft robotics. Recent applications include wearable devices for sensing mechanical changes, temperature, humidity, and chemicals,[6–13] stretchable radio frequency (RF) receivers,[14] reversibly deformable and mechanically tunable fluidic dipoles, loops, monopoles and patch antennas, split-ring resonators,[15–17] as precursor for ITO electrodes,[18] for interconnects and soldering,[19] embedded stretchable and elastic conductors,[20,21] superconducting micro/nanoelectronics,[22] self-healing elastomer composites,[23] as field-controlled electrical switches,[24] LM enabled pumps,[25] ferrofluidic magnetocaloric devices,[26] for energy harvesting,[27,28] as self-healing anode for lithium-ion batteries,[29] and even tumor-targeting theranostic applications.[30] With this wide and diverse range of applications, the issues of direct writing, patterning, and processing of LMs has received considerable

N. Hussain, T. Fu, Dr. G. Marques, Dr. T. Scherer,
Prof. J. Aghassi-Hagman, Dr. M. Hirtz
Institute of Nanotechnology (INT) and Karlsruhe
Nano Micro Facility (KNMF)
Karlsruhe Institute of Technology (KIT)
Hermann-von-Helmholtz-Platz 1 76344, Eggenstein-Leopoldshafen,
Germany
E-mail: jasmin.aghassi@kit.edu; michael.hirtz@kit.edu
Dr. C. Das
Institute for Applied Materials (IAM-ESS)
Karlsruhe Institute of Technology (KIT)
Hermann-von-Helmholtz-Platz 1 76344, Eggenstein-Leopoldshafen,
Germany

Dr. U. Bog
n.able GmbH
Hermann-von-Helmholtz-Platz 1 76344, Eggenstein-Leopoldshafen,
Germany

L. Berner, Dr. I. Wacker, Prof. R. R. Schröder
Cryo Electron Microscopy
Centre for Advanced Materials (CAM)
Heidelberg University
Im Neuenheimer Feld 225 69120, Heidelberg, Germany

Prof. R. R. Schröder
3DMM2O Cluster of Excellence (EXC_2082/1-390761711)
and Cryo Electron Microscopy
BioQuant
Heidelberg University
Im Neuenheimer Feld 267 69120, Heidelberg, Germany

Prof. J. Aghassi-Hagmann
3DMM2O Cluster of Excellence (EXC_2082/1-390761711) and
Department of Electrical Engineering and Information Technology
Offenburg University of Applied Sciences
Badstraße 24 77652, Offenburg, Germany

critical attention, and is an area of highly active research. Despite its ductile and fluidic nature, favoring printability, LMs suffer from a significant drawback: the particular combination of viscosity, surface tension, and density makes them hard to print with inkjet printing or any other standard direct writing methods reaching resolution in the low-micrometer range. While a diverse set of alternative lithography approaches can be employed and can reach even sub-micron resolution, these approaches are usually based on stencils, mask, or templates and/or require sophisticated photolithography, electron beam lithography, or hybrid approaches.[31] As these complicate fabrication and design changes and require much more complex and expensive infrastructure, the direct write additive methods still raise broad interest for the patterning of LM. Recently, some progress was achieved toward this challenge: Tabatabai et al. demonstrated microcontact printing of eutectic gallium-indium (EGaIn) and Galinstan (brand name for eutectic gallium-indium-tin) and successfully patterned dot arrays, lines, and pads and also presented a functioning elastic soft capacitor.[4] These alloys are of particular interest for applications, as of combining high conductivity, liquidity at RT, and low toxicity (which in contrast, for example, forbids the use of Hg in real-world applications). Similarly, Boley et al. reported a direct writing method for gallium-indium based inks in which the LM ink is printed on substrate using a syringe pump, and a computer-controlled stage providing patterns with micron scales.[32] Nozzle based LM deposition can even result in 3D structures: the oxide layer building up on Ga-In-Sn based alloys under ambient conditions, though being only 1–3 nm thick,[33–36] provides sufficient stability to structures which would ordinarily be untenable due to the extremely high surface tension (>500 mN m^{-1}).[37–39] However, at the same time, this oxide layer is further complicating printing of gallium-based LM alloys, thus is removed with HCl or NaOH treatment in some approaches.[38,40] Free-standing mm-scale 3D structures were demonstrated by Ladd et al. at RT by pushing Ga–In alloy through a capillary and stacking droplets of LMs on top of each other forming filaments and other arbitrary 3D structures.[41] Recently, Park et al. demonstrated LM printing for microscale 3D interconnects for stretchable integration of electronics. Here, instead of depositing single droplets, low rates of motion while printing allows printed features to be lifted off from the surface, remaining stable while being placed at a different location to form 3D interconnects.[19]

The presented LM printing methods have—as a general virtue of direct write methods—the advantage of depositing material only where it is needed, thus using less material and generating less waste, as compared to subtractive methods which must start with complete surface coverage and remove material to form the desired patterns. Unfortunately, these LM direct printing methods were never examined for their potential application in fully functional, printed electronic devices that utilize the inherent desirable attributes of LMs. In our work, we present a glass capillary-based direct-write method for printing LMs, exploring this potential for fully printed LM-enabled devices. Examples of resistors, p–n diodes, and field effect transistors (FETs) show that the potential of LM printing is far exceeding the use of interconnecting conventional electronic devices in PE.

2. Results and Discussions

2.1. Printing Method and LM Example Structures

As LM ink, commercially available Galinstan alloy was used. Galinstan is ductile and fluid at RT (as it melts between −10 and −19 °C) so it can be easily dispensed, deformed, and stretched. **Figure 1** represents a schematic image of the glass capillary-based direct printing system. The system is based on a customized commercial nanolithography system that provides a five-axis stage with automatic movement in the x, y, and z-axis and two tilting axes in the xy plane. This system is customized with a glass capillary mounted on a static holder, a syringe as an ink reservoir, and a syringe pump. The glass capillaries were prepared with long tapers (around 9–15 mm) and small tips (around 1 µm) using a pipette puller at appropriate operating parameters. To obtain bigger tip openings (20–100 µm), the glass capillary was scored at a position of matching width by moving above the desired score location and push with a smooth and continuous motion to break the glass. After mounting and filling of the glass capillary with the LM, printing is achieved by depositing the LM with the glass capillary in close proximity to a moving target substrate. The LM flow rate is controlled through the syringe pump while the glass substrate mounted on the nanolithography stage moves at a controlled speed under the stationary glass capillary held at a controlled standoff distance above the substrate.

Many factors influence the dimensions of the written patterns, for example, the inner diameter of the capillary, the size of capillary tip opening, and the distance between the substrate and the glass capillary tip. For reliable patterning, the distance between the glass capillary tip and the substrate is varied from 0 (touching the surface) to 5 µm with respect to the size of the tip. Dispensing LM from the tip results in an increase of the LMs surface area, thus, the oxide layer must first be ruptured and then reforms after printing on the substrate. For each capillary, the flow rate of the syringe pump is optimized to ensure proper extrusion of LM to form a continuous deposition and avoid droplet formation on the capillary tip. Typical parameter ranges to bring LM at the glass capillary tip were 5 to 100 µL min^{-1}. After this initial conditioning, the flow rate was maintained low enough to hold the LM at the capillary tip and patterns are fabricated by bringing the tip in close proximity to the substrate. While coating of capillary with Au can improve the flow of LM,[42,43] we generally omitted such coatings here, to avoid amalgamation.

Figure 2 shows some typical outcomes for line patterns. Glass slides of 1.8 mm × 1.8 mm were used as substrates here and the results signify that complex interconnect patterns or designs of electric circuits can be printed with high resolution with the setup. These patterns can span over more than 1 cm with high uniformity in line width (Figure S2, Supporting Information). The minimum width of homogeneous, well-defined lines achieved in our approach is (1.3 ± 0.1) µm (Figure S2, Supporting Information), slightly smaller than in previous reports.[19,32,43,44] This high-resolution LM deposition was achieved using a tip of 2 µm opening and a writing speed of 1000 µm s^{-1}. Printing velocity and tip size can further control the width of the lines. Using the same tip opening size,

**ADVANCED
SCIENCE NEWS**

www.advancedsciencenews.com

**ADVANCED
MATERIALS
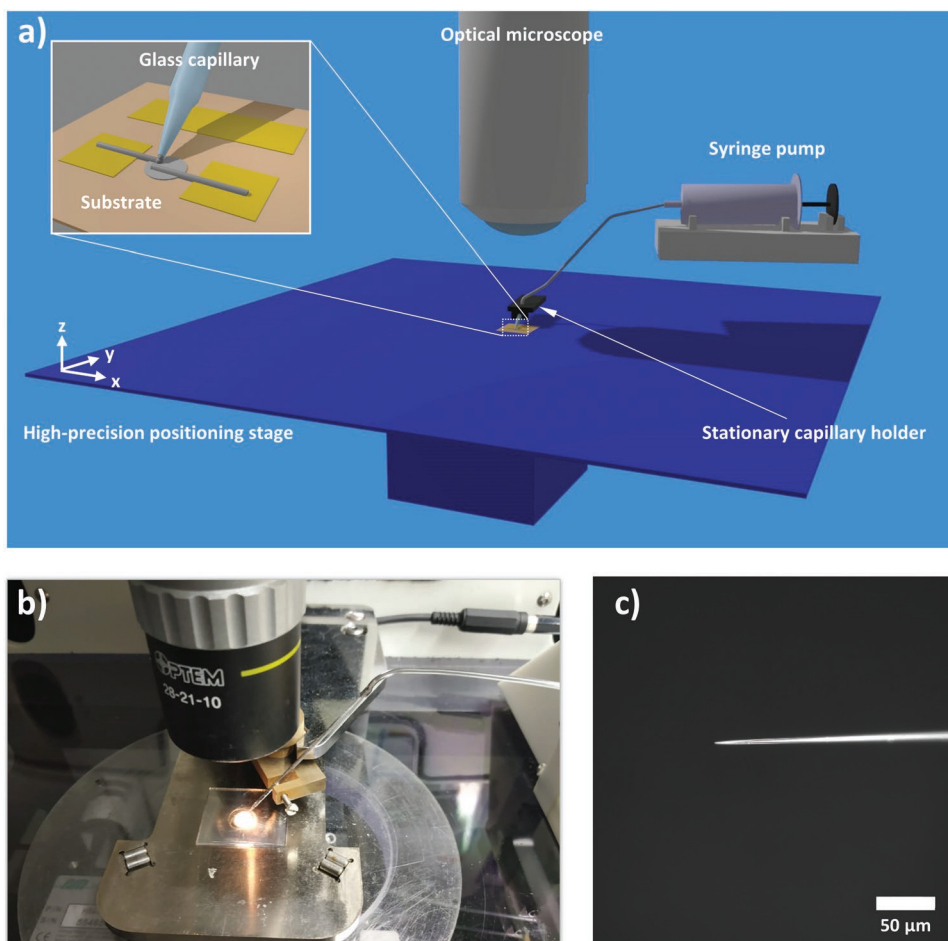TECHNOLOGIES**

www.advmattechnol.de

Figure 1. Scheme of the printing setup. a) Schematics of the printing setup consisting of a high-precision positioning stage, an optical microscope for monitoring, and a stationary holder for a glass capillary that is connected to a syringe pump for controlled release of LM. The inset shows a close up of the glass capillary writing a lipid metal line onto a substrate by moving the position stage appropriately in *x*, *y*, and *z* directions. b) Actual image of the glass capillary in the holder, positioned over a glass sample used as substrate. c) Microscopy image of a glass capillary prior to opening up the tip aperture.

faster writing speeds generally result in a narrower line width, but can also lead to discontinued lines. Also, the line width increases with increasing tip opening size (Figure 2f). Interspacing of lines can be achieved in sub-10 µm range without merging of lines (Figure S3, Supporting Information). The results show that low-microscale yet cm-scale spanning intricate designs can be achieved with this method, without need for micro-machining, masks, or molding processes. This also facilitates reduction of waste material, for example, while filling microchannels for applications.[15,45]

The remarkable stability of Galinstan-based LM structures, allowing even for 3D free standing arcs (Figure 2d; Figure S4, Supporting Information), as also demonstrated for LM droplets[41] and interconnects,[19] is based on an oxide layer "skin" forming immediately on contact with oxygen from environmental air. In order to obtain a better understanding of the oxide layer formation and in particular learn about the thickness of the layer, we conducted characterization of the printed LM lines with time-of-flight secondary ion mass spectrometry (TOF-SIMS) and X-ray photoelectron spectroscopy (XPS), results shown in **Figure 3**.

The oxide layer can clearly be detected in TOF-SIMS measurements (Figure 3a–c). For this, a cross section of a LM line was done at −100 °C (Figure 3a) and then an image area with parts of the cross section and parts of the LM line surface (Figure 3b) was mapped by TOF-SIMS (Figure 3c). While the cross section shows no GaO$^-$ signal (as indicator of gallium oxide), a signal is clearly observed on the surface areas where the oxide layer is still present. During TOF-SIMS milling, the signal quickly diminishes within few frames (Figure 3c), indicating the thin nature of this layer. For further information on the oxide layer thickness, XPS measurements from a one month air-aged Galinstan sample deposited on Si were conducted (Figure 3d). The Ga3d core level spectra has two high-intense peaks at 20.9 and 18.6 eV corresponding to the Ga^{3+} and Ga^0 states of Ga.[34,46] This clearly indicates the Galinstan surface oxidized and formed Ga$_2$O$_3$. Additionally, In3d and Sn3d peaks are also detected on the oxidized surface of the Galinstan (see Figure S5, Supporting Information). To determine the thickness of the surface Ga$_2$O$_3$ layer, we performed a sputtering depth profile using 500 eV monoatomic Ar ion sputtering. The relative intensities of Ga^{3+} and Ga^{0+} states in the Ga3d core level
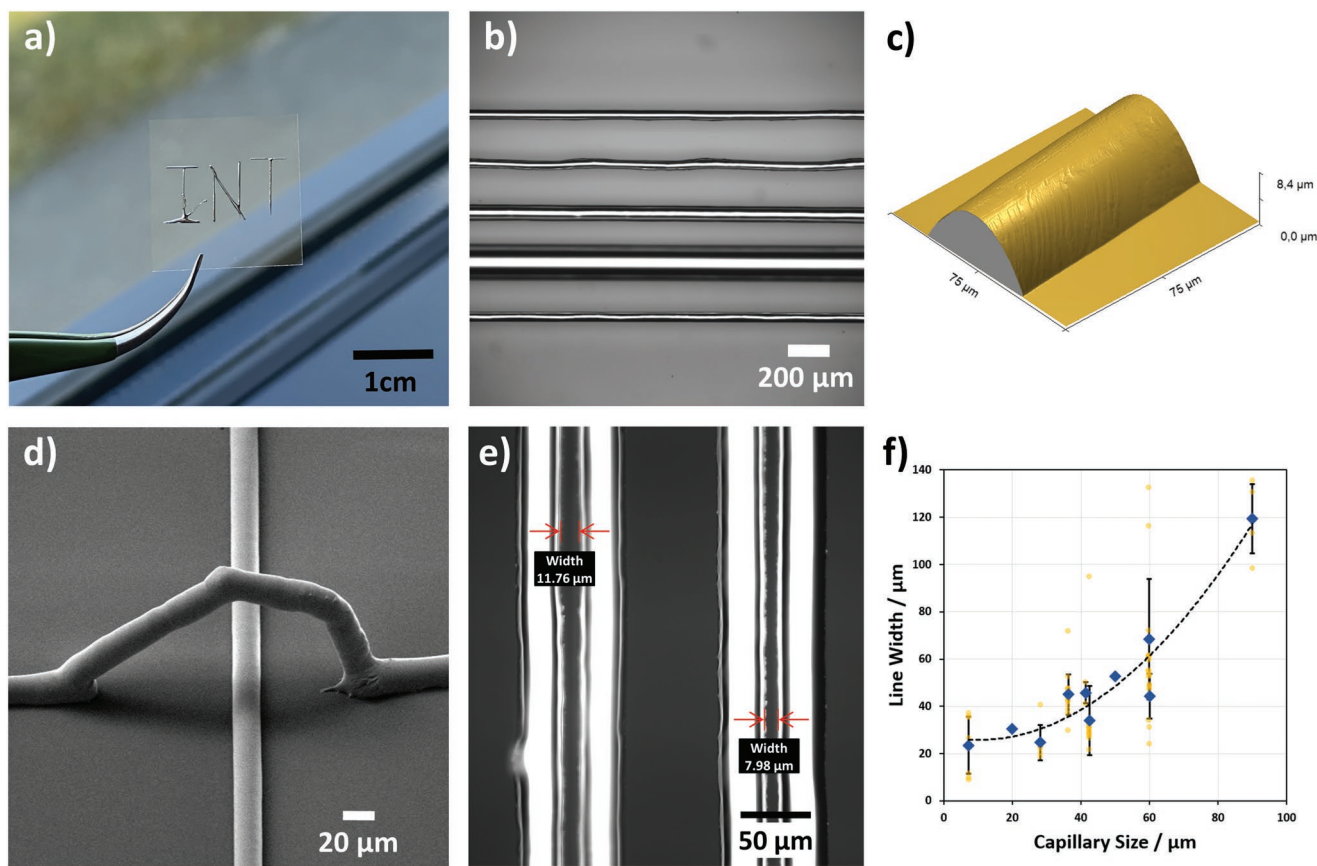
Figure 2. Line printing with Galinstan. a) Macroscale patterning of the letters INT on a glass cover slip. b) Example of LM lines with different width obtained by tuning writing velocity. c) AFM image of a LM line. d) SEM image of an Galinstan line arching over another previously printed line. e) Parallel lines with different length gaps in between. f) Resulting line widths versus tip opening size. The blue diamonds show average line widths obtained from 10 different capillaries (yellow circles show distribution of obtained lines, error bars represent S.D.). The dashed line is a polynomial fit ($y = 0.0144x^2 - 0.2945x + 27.363$, $R^2 = 0.9184$) for guiding the eye.

spectra are considered for the determination of Ga_2O_3 surface layer thickness. From the XPS data, a thickness in the range of 2.5 to 3.5 nm is obtained via modeling the data in regard to the theoretical ratio of Ga3d peak intensities in infinite thick Ga and Ga_2O_3 films (details are given in the Supporting Information). Following the evolution of the oxide layer thickness on a sample from freshly prepared up to 60 days (Figure S6, Supporting Information), there was only a minor growth of film, about 0.5 nm, in this time period. Thus the initial oxidation of the surface limits the further oxidation of Galinstan, and the air aging has only a minimal effect on the growth of Ga_2O_3 on it. A detailed analysis is given in the Supporting Information. Overall, our results confirm the nanometer-sized thickness of the native oxide layer as also estimated in other studies.[33,36]

In order to expand the LM-direct writing techniques to fully printed electronic devices, we have focused on the fabrication and functionality of resistors, diodes, and FETs. These devices are particularly interesting for the development of bioelectronic applications[47–49] and wearables[9,10,50] where large numbers of them are placed in active arrays and microelectrode applications.[51,52] In the following we present results on I) LM interconnects and resistors, II) fully printed diodes, and III) fully printed transistor structures.

2.2. LM Interconnects and Resistors

As a first test of the use of the obtained LM structures for printable electronic applications and to probe stability for later uses, the electrical resistance of as-printed and poly(methyl methacrylate) (PMMA) encapsulated LM lines were characterized. For this, Au electrodes with different distance were fabricated with laser ablation (details in Experimental Section). After sonication in isopropanol and water for 2 min each, LM was printed with the described direct writing method. **Figure 4** shows an optical microscopy image of a typical printed resistor. Similar resistors with varying length l and width w were characterized. The height h of the obtained structures was measured with a profilometer.

The absolute resistance R of the resistor structures was determined using two-probe measurements. All measurements were recorded at RT and within eight hours after LM printing. Measurements were done in triplicate from three different samples and ρ is calculated from the measurements by

$$\rho = R\frac{A}{l} \approx R\frac{wh}{l} \qquad (1)$$

**ADVANCED
SCIENCE NEWS**
www.advancedsciencenews.com

**ADVANCED
MATERIALS
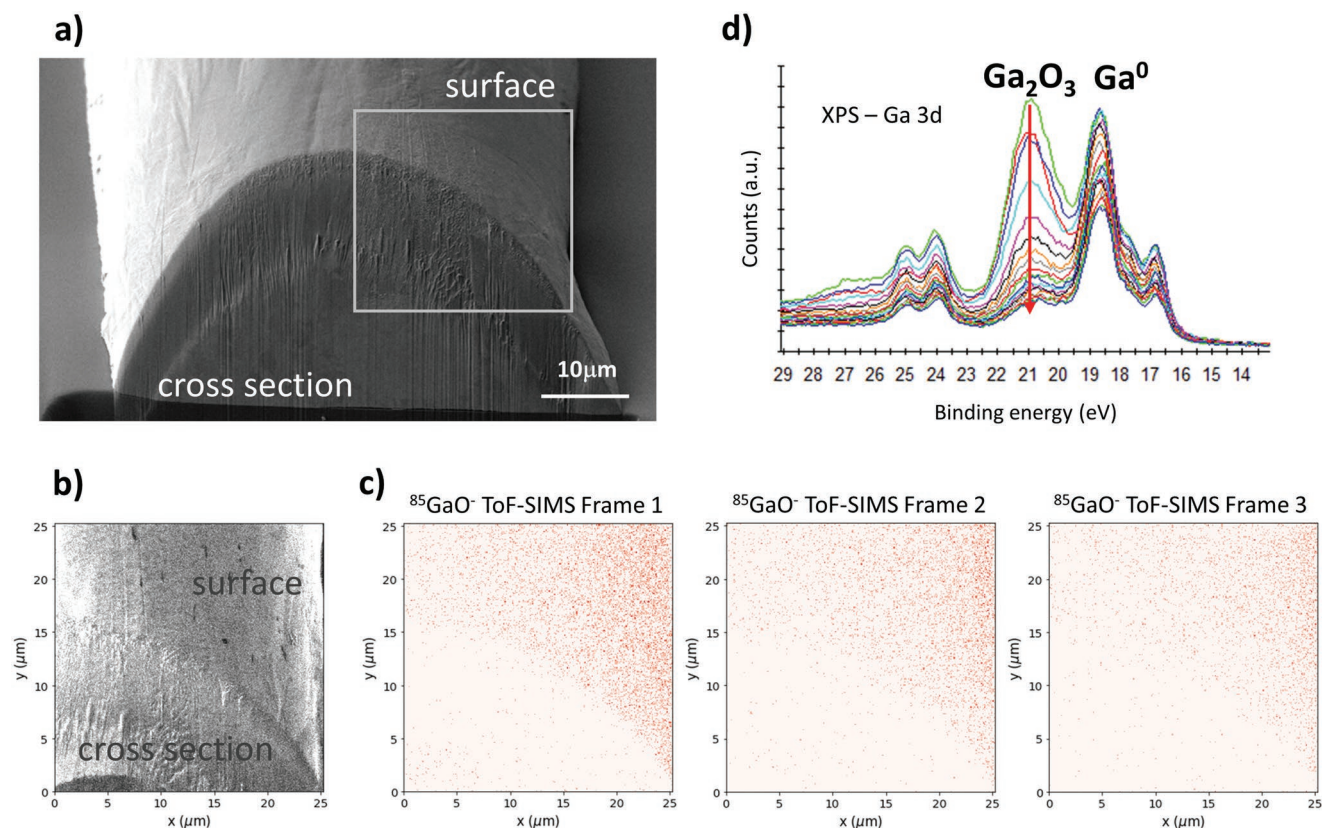TECHNOLOGIES**
www.advmattechnol.de

Figure 3. Chemical analysis of oxide layer on the printed LM lines. a) SEM secondary electron (SE) image of a cross section after TOF-SIMS analysis (executed on area indicated by grey frame). b) FIB SE image of the first frame of the TOF-SIMS analysis. c) GaO⁻ signal of the first 3 ToF-SIMS frames indicating an oxide layer on the sample surface while the in situ milled cross section (not previously exposed to air) shows no sign of an oxide cover. d) Ga3d core level spectra from XPS measurement on a one month air-exposed Galinstan sample.

where R is the measured absolute resistance, A is the area of the cross section, w is width, l is length, and h is the height of the printed interconnect/resistor. The obtained data are plotted in Figure 3c, showing the calculated ρ for resistor structures of different lengths l. The area A can be approximated by $w \times h$ as the profilometer measurements reveal that for the relevant line widths, the curvature of the resistor lines is flattened to an extent that the cross-sectional area can be calculated as rectangular.

The material parameter ρ is expected to be constant. However, our plot reveals that in the case of the resistor structures, ρ is significantly higher for short resistors, and decreases as the length of the resistor increases. Above 150 to 225 µm in length, the change in ρ is insignificant, and converges to a value that is just ten times lower than for bulk Galinstan.[53,54] The raised ρ for small resistor lengths can be attributed to an artifact due to contact resistance at the Au/Galinstan interface (Figure 4d). In this image, also a phase separation of the LM is visible as light and dark shaded areas in the cross sections. This separation is caused by the cooling of the LM for the cross sectioning, as at RT, EDX shows a smooth and homogeneous chemical distribution (Figure S7, Supporting Information). For smaller resistor length, the contact resistance is dominating the overall resistance, while for longer resistor structures it becomes negligible. Overall, the Galinstan retains a high electrical conductivity after

processing with the capillary printing, almost on par with bulk Galinstan and far exceeding other printable materials.

While being liquid is key for the processing of LMs and makes a big part of the appeal of such materials for applications, it also potentially is a source of concern in regard to stability, especially for structures built by additive manufacturing as discussed here. Therefore, encapsulation of the structures after printing and its influence on electrical properties was probed for the resistor structures. Here, (PMMA) was chosen, as, in addition to a mechanical protection, it can also act as a good barrier against oxygen and moisture. After completion of the first round of resistance measurements, PMMA was spin-coated on the substrates at 4000 rpm for 1 min, resulting in encapsulation of the LM resistor structures. After PMMA encapsulation, electrical resistance measurements were again conducted for the same resistor structures as before. All structures survived encapsulation, showing the relatively high mechanical stability of the LM due to the built-up oxide layer. Resistor structures of smaller length showed some minor increase in ρ and a higher variability (indicating that here the influence of encapsulation is most prominent), while for all structures longer than 150 µm no significant change in ρ was observed due to encapsulation. These results show that encapsulation of printed LM structures is feasible and can be used to protect printed devices in applications if necessary.
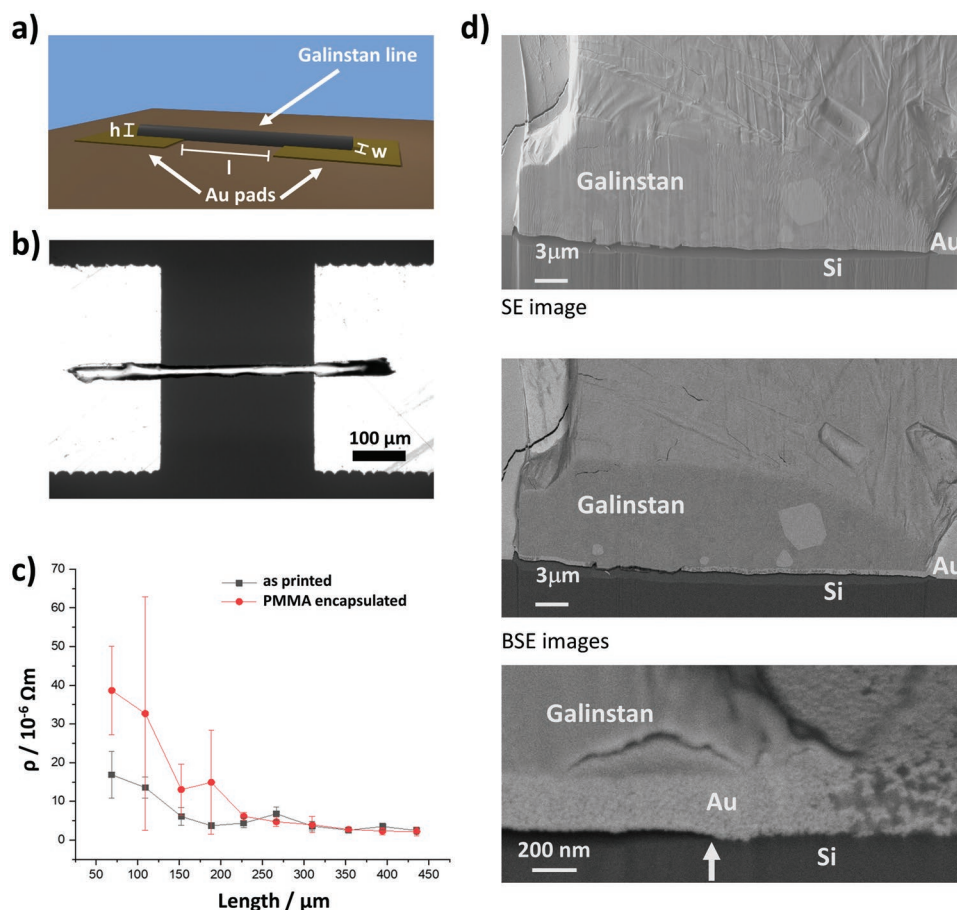
Figure 4. Characterization of LM resistor structures. a) Schematic of the Galinstan line printed over two gold pads. The distance between the gold pads defines the length l of the resistor structure, line width w, and height h are measured by optical microscopy and profilometry, respectively. b) Optical micrograph of a typical resistor structure. c) Graph of specific resistance ρ for resistor structures of different length. d) FIBSEM analysis of a galinstan line printed on a gold pad: SEM secondary electron (SE, top), and backscattered electron (BSE, bottom two) images of a cross section through a Galinstan line show good contact between Galinstan and gold while the entire assembly lifted off the Si substrate during freezing (left of arrow) due to the larger thermal expansion coefficients of gold and Galinstan.

2.3. Fully Printed Diode

Oxide semiconductors were studied widely in PE due to their high electron mobility, transparency, and easy printability. Whereas oxides are naturally n-type materials, they may also act as p-type semiconductors but with relatively lower mobility. Printed p–n diodes have shown excellent ON/OFF ratios in the range from 0 to 5 V with diode threshold voltages around 1 V.[55] However, these devices make use of ITO sputtered electrodes which was replaced in this work by LM-printed electrodes. Due to their elongated shape, these printed electrodes serve at the same time as intra-connecting wires in the fully printed diodes.

Here we fabricated p–n diodes based on oxide semiconductors (printed by inkjet printer on a glass substrate) and capillary printed Galinstan lines with gold electrodes. The n-type semiconductor film is based on an indium oxide precursor solution and was printed on top of the Galinstan line which acts as the cathode of the diode. The printing process was carried out on a 60 °C heated printing stage and the substrate was dried after printing at 100 °C for 10 min. Afterward, the p-type semiconductor film, in form of CuO, was printed on top of the

In_2O_3 layer at 60 °C and then dried for 10 min at 100 °C. Subsequently, the substrate was annealed at 400 °C, for 2 h. Last, the conductive polymer poly(3,4-ethylenedioxythiophene) polystyrene sulfonate (PEDOT:PSS) was printed on top of the CuO film and connected to the anode, based on gold. The device fabrication process is illustrated in **Figure 5**.

The output characteristics of the diode were measured by sweeping the voltage from −10 to +10 V at the anode. The cathode of the diode is grounded. With the approximated p–n-diode area of 130×60 μm^2, the output in Figure 5c shows that the current density of the Galinstan connected diode is relatively high compared to previous work (0.77 A·cm^{-2}).[55] Our results have shown currents in the order of $I_{ON} = 10^{-4}$ A and $I_{OFF} \approx 10^{-9}$ A, translating to a current density of ≈2.28 A cm^{-2}, at an area of 100×100 μm^2. This larger value in current density is the result of the improved performance related to the high conductivity of Galinstan combined with gold electrodes. Despite the satisfying I_{ON}, the current in the reverse region is quite high, which can be caused by pore formation, during the annealing step of the oxide films. The PEDOT:PSS likely penetrated those pores and resulted in leakage currents. This
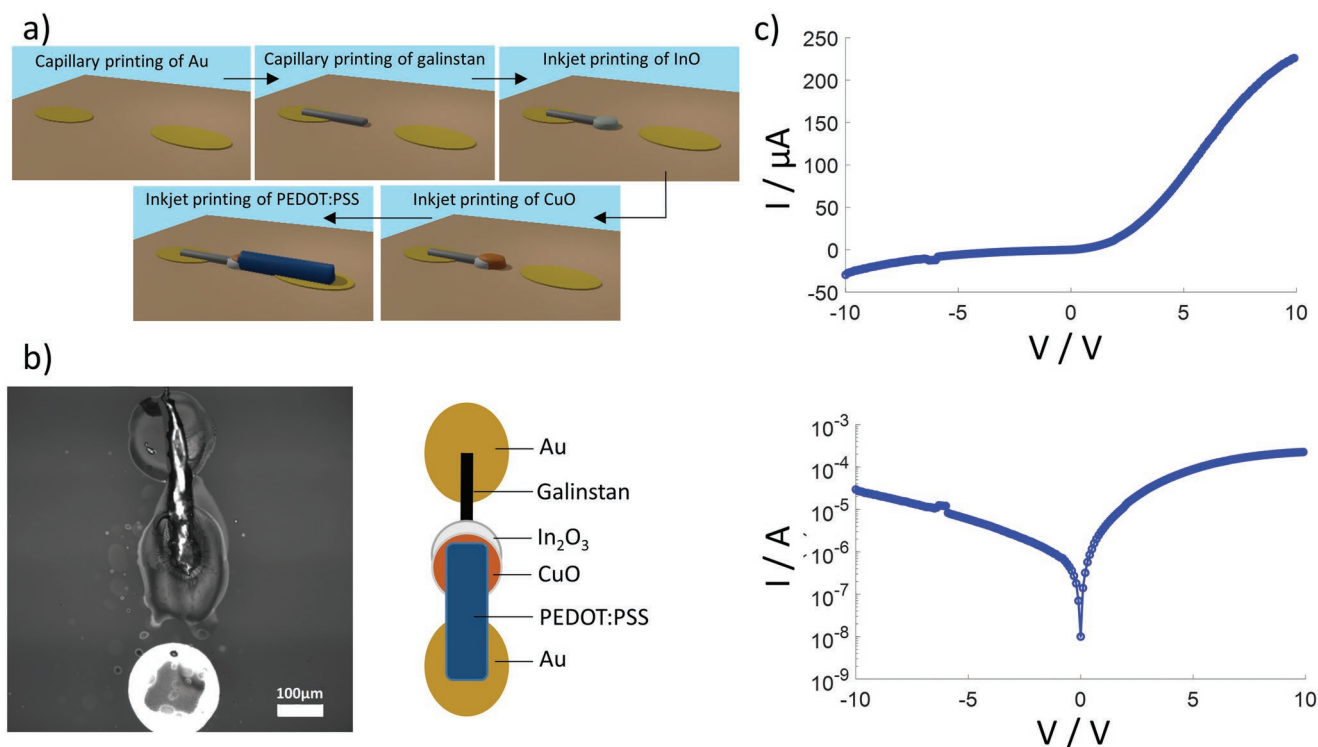
Figure 5. Characterization of fully printed diode. a) Workflow for the construction of a fully printed diode by combining capillary and inkjet printing. b) Optical micrograph of a typical printed diode (left) and the corresponding schematic (right). c) Typical I–V characteristics of the printed diode in linear (top) and log-scale (bottom).

might, however, be avoided by engineering and printing process optimization.

2.4. Fully Printed Transistor

Next we developed a fully printed transistor based on our prior work on partially printed electrolyte-gated field effect transistors (EGTs), where all electrodes have been structured by lithography based on sputtered ITO on glass.[56,57] These EGTs showed higher gate capacitance compared to dielectrically gated, conventional ones, due to the formation of a Helmholtz double layer. The high area-specific capacitance enables a low-voltage operated device with high ON-current.[58] As in the case of the p–n diodes, we used an indium oxide (In_2O_3) precursor solution, annealed at 400 °C to form the n-type channel material for EGT. These channel materials feature high field-effect mobility (>30 cm^2 V^{-1} s^{-1}), therefore high I_{ON}/I_{OFF} ratios at low voltage levels are feasible.[59]

For the fully printed transistors, the substrate was structured with capillary printed gold electrodes and Galinstan conductive lines, which are extended from the drain and the source gold electrode. Then In_2O_3 as n-type semiconductor channel was printed via glass capillary in between the extended Galinstan lines. Then, the substrate was annealed at 400 °C for 2 h. Afterward, a composite solid polymer electrolyte (CSPE) was printed by inkjet printing on top of the indium oxide channel. This layer partially covers the Galinstan line that is attached to the channel. Subsequently, the conductive polymer (PEDOT:PSS)

was inkjet printed on top of the CSPE layer and connected to the gate electrode pad. The printing process of the transistor is illustrated in **Figure 6**a with the microscopy picture of the transistor's top view shown in Figure 6b.

The transistor was characterized by a semiconductor parameter analyzer at RT with 50% humidity level, and a gate voltage (V_{GS}) sweeping from −1 to 1 V. As the transfer and output characteristic curves given in Figure 6c show, the transistors display a negative threshold voltage (V_T) of −0.31 V, and a current ON/OFF ratio of 1.84×10^3. It was also observed that there is a leakage current in the order of 10^{-8} A. The thickness of the electrolyte layer on top of the Galinstan lines is thinner, so that PEDOT:PSS might penetrated the electrolyte in these areas, causing this significant leakage current. This might be improved by future optimization of the printing process, also addressing the yield (≈19%) of obtained transistors.

However, if a high yield, and also higher performance is required, the Galinstan can be replaced with gold. For a normally-OFF transistor with V_T of 0.206 V and a normally-ON transistor with a V_T of −0.211 V, the transfer curves are shown in **Figure 7**a,b, respectively. For reliable circuit designs, both, normally-ON and normally-OFF operation modes, are essential. The subthreshold slope is comparable in both cases, ≈98 mV dec^{-1} (normally-OFF) and (≈109 mV dec^{-1}). Nevertheless, the fabricated all-gold printed devices demonstrated better reproducibility with a yield of ≈82%. A current leakage of ≈10^{-7} A was observed, which is higher compared to the Galinstan based transistors, however, this is expected, since the current driving capability in gold is higher than in Galinstan.
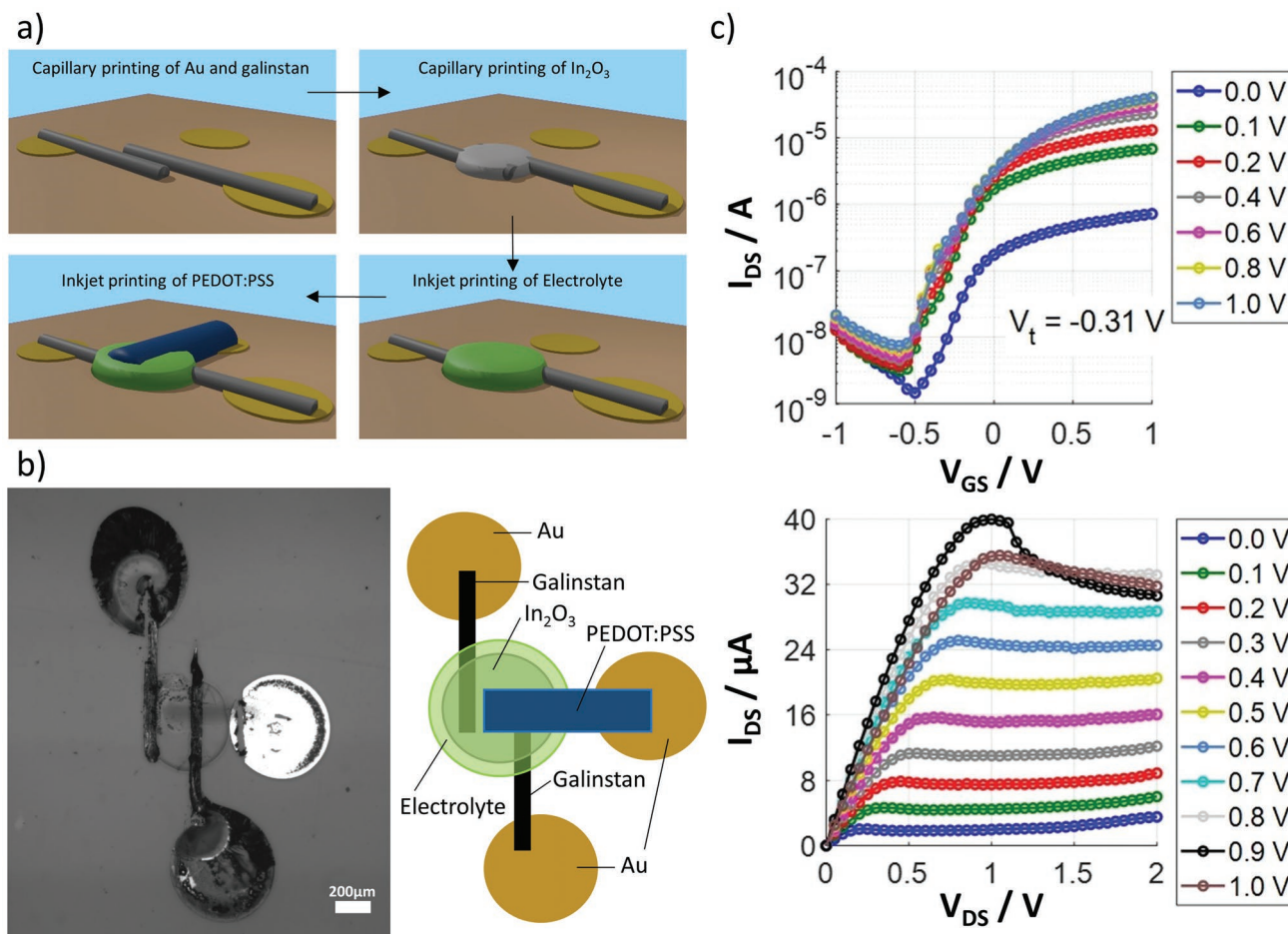
Figure 6. Characterization of fully printed transistor. a) Workflow for the construction of a fully printed FET by combining capillary printed Galinstan lines and inkjet printing for the materials In_2O_3, PEDOT:PSS, and electrolyte. b) Optical micrograph of a typical printed FET (left) and the corresponding schematic (right). c) *I–V* characteristics of the FET for voltage applied to ground/source (top) and drain/source (bottom), respectively.

3. Conclusion

In summary we have shown that Galinstan capillary printing represents a versatile LM printing process enabling the fabrication of various fully printed devices. We have fabricated and analyzed the electrical behavior of interconnect wires, resistors, p–n diodes, and transistors which are in principle process compatible with other digital printing methods and thin film structuring methods for integration. Our results demonstrate working p–n diodes with ON/OFF ratio of 10^5, fully printed
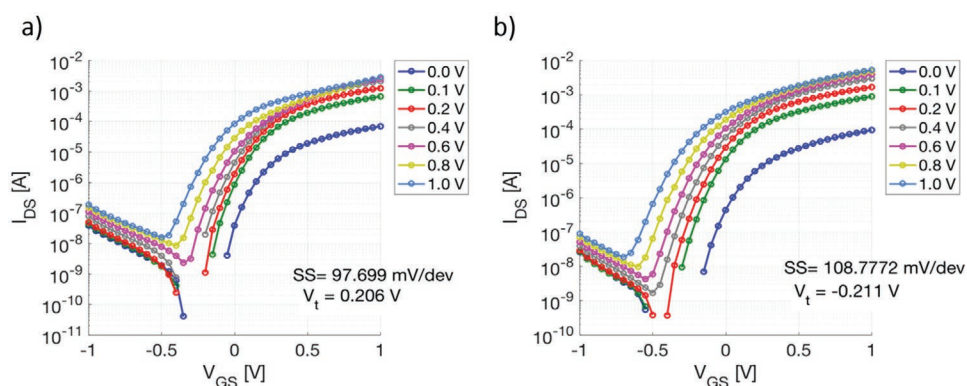

Figure 7. Characterization of fully printed transistors with Au electrodes. Transfer characteristics, of the transistor operating in a) normally-OFF mode and b) in normally-ON mode.

ADVANCED
SCIENCE NEWS

www.advancedsciencenews.com

ADVANCED
MATERIALS
TECHNOLOGIES

www.advmattechnol.de

transistors with ON currents in the order of tens of mA and tunable resistors that can be further encapsulated with PMMA to protect them from environmental influences without losing conductivity. The device functionality achieved with only a single processing technique for various inks eases the fabrication flow and shows the great potential of LM printing which is by far exceeding its simple use as interconnect of conventional electronic devices in PE. We believe that in the future these fully printed devices can be used in circuit building blocks for wearable, flexible sensors, and in particular for bioelectronic and biomedical applications. In the latter the devices will be in direct contact with living systems and the favorable material properties in regard to toxicity as well as their relatively low cost of processing (enabling one-time-use when needed) will be a significant advantage.

4. Experimental Section

Preparation of Nozzles: A Sutter Instruments P-1000 micropipette puller system was used to prepare glass capillaries with different tip and taper size. Glass pipette without filament from Warner Instruments (GC120TF-10) were used whose outer and inner diameter were 1.2 and 0.94 mm, respectively, the length being 100 mm. Pulling parameters for heat, filament (fil), velocity (vel), delay (del), and pull were also tried for different tip and taper sizes.

Preparation of Galinstan Ink: Galinstan consisting of 68% gallium, 21% indium, and 11% alloy by weight was obtained from Strategic Elements, Germany, and used as received.

Preparation of In_2O_3 Ink: In_2O_3 ink preparation was adapted from a previous recipe:[60] a solution of 0.05 M $In(NO_3)_3 \times H_2O$ in double deionized water was prepared. Then glycerol was mixed in with a ratio of 4:1. For achieving a homogenous mixture, the ink was stirred again at RT and passed through a hydrophilic 0.2 μm polyvinylidene fluoride (PVDF) syringe filter before printing.

Preparation of CuO Ink: The CuO precursor ink preparation was adapted from a previous report:[61] a solution of 0.1 M $Cu(NO_3)_2 \times 2.5\ H_2O$ was prepared in double deionized water. Then glycerol was admixed in a ratio of 4:1. The CuO precursor was also stirred at RT and filtered through a 0.2 μm PVDF syringe filter before printing.

Preparation of CSPE Ink: CSPE ink was prepared as described previously.[60] In short, 4.29 wt% polyvinyl alcohol was dissolved in 85.71 wt% dimethyl sulfoxide and stirred for two hours at 90 °C. At the same time, 1 wt% lithium perchlorate ($LiClO_4$) was dissolved in 9 wt% propylene carbonate and stirred for two hours at RT. Both solutions were mixed together by stirring at RT. As last step, the solution was filtered through a 0.2 μm polytetrafluoroethylene membrane.

Preparation of PEDOT:PSS Ink: The PEDOT:PSS ink was prepared as previously described.[60] For the top-gate ink, 70 wt% PEDOT:PSS was stirred together with 30 wt% ethylene glycol for 2 h. Directly before printing, the ink was filtered with a 0.45 μm PVDF membrane.

Preparation of Substrates: Standard glass coverslips from VWR Germany were cleaned with chloroform, 2-propanol, and deionized water, dried by blowing with nitrogen, and in some cases for hydroxyl functionalization of the surface, substrates were cleaned with oxygen plasma (10 sccm O_2, 0.2 mbar, 100 W, 2 min) in a ATTO B plasma-cleaner (Diener electronic GmbH, Germany).

Printing Setup: A printing setup as schematically shown in Figure 1 was used for all the direct writing experiments. Lines of Galinstan were directly printed using a stationary glass capillary mounted in a modified NLP 2000 nanolithography system (NanoInk, USA) that offers a sample stage that could translate in *x*, *y*, and *z* direction and a microscope for optical surveillance of the printing process from above the sample. A custom holder was designed and self-built to mount the glass capillary

used for printing. Glass capillary and syringe pump were connected with LDPE tubing (RCT Reichelt Chemietechnik GmbH Co) of inner diameter of 0.1 mm and outer diameter of 3 mm. For each experiment, the syringe was filled with Galinstan, which works as an ink reservoir and the ink was pushed from syringe to glass capillary via LDPE tubing at a constant flow rate (around 10 μL min^{-1}, tuned to achieve a stable filling) as shown in Figure 1. The height between the tip of the glass capillary and the substrate was held constant for each experiment, and the system's optical microscope was used for visually monitoring the tip interaction/distance with the glass substrate. The distance between the tip and substrate was varied in between experiments from directly touching the surface to a 5 μm distance depending on the opening size at the tip of the glass capillary. For printing, first of all, the stage was moved to the starting point of the pattern. Upon reaching the starting position, the tip of glass capillary was brought in contact with the substrate or kept at a certain height from the substrate according to tip size. Printing was then initiated by bringing the capillary into contact with the surface and the pre-programmed stage movements to form the desired pattern were started. Once the pattern was finished, the stage was moved down (around 200 μm) quickly, effectively separating the glass capillary from the pattern.

Galinstan Interconnects Fabrication: A glass substrate coated with 150 nm Au over a 7 nm Cr layer for better adhesion was structured with a TRUMPF TruMicro 5000 laser ablation system for obtaining contact pads with varying distances between the pads (60–550 μm). The Au structures serve as the contact pads for the printed Galinstan interconnects. After laser structuring, the substrates were rinsed with 2-propanol and deionized water, then dried by a stream of nitrogen. Subsequently, the Galinstan interconnects were printed on the customized nanolithography system described above

The capillary was filled with Galinstan by applying pressure through the syringe pump. The patterns were completed at different writing speed from 200 to 1000 μm s^{-1}. For each experiment, freshly cleaned glasses were used. After printing, the interconnects were characterized in optical microscopy and by resistance measurements.

Scanning Electron Microscopy Imaging and Focused Ion Beam Sectioning: To create cross sections of Galinstan lines on a silicon substrate as presented in Figures 3,4 a dual focused ion beam (FIB)/scanning electron microscopy (SEM) microscope (Crossbeam 540, Carl Zeiss Microscopy, Oberkochen, Germany) was cooled down to −100 °C using a Leica cryo-stage. This resulted in solid Galinstan amenable to ablation with Ga$^+$ ions. FIB Ga$^+$ ions with an energy of 30 kV and currents of 15 nA, 3 nA, and 700 pA were used for milling and polishing the cross section. SEM images were recorded using a primary electron energy of 3 keV and a current of 500 pA by imaging SEs (topological contrast) and/or backscattered electrons (material contrast).

The SEM and FIB measurements for Figure S7, Supporting Information were performed using a dual beam Zeiss AURIGA 60 system. SEM imaging was carried out using an e-beam with 5 kV and an aperture of 30 nA. For cross sectioning and trench milling a focused Ga-ion beam with 30 kV and distinct apertures in the range of 20 pA to 16 nA was applied. Partially cross sections were milled and imaged under cryo-conditions using a Deben cryo-stage enabling measurements at −50 °C.

Time-of-Flight Secondary Ion Mass Spectrometry: A ToF-SIMS analysis system (Tofwerk AG, Thun, Switzerland & Carl Zeiss Microscopy, Oberkochen, Germany) attached to the Crossbeam540 was used for TOF-SIMS analysis: The sample was tilted to 54° and irradiated with Ga$^+$ ions (30 keV, 50 pA). Secondary ions originating from the ion-sample interaction were detected and imaged. The maps showed the spatially distributed secondary ion signal of the ToF-SIMS detector integrated over a mass/charge ratio between 84.5 and 85.5, corresponding to $^{85}GaO^-$ ions.

Energy-Dispersive X-Ray spectroscopy: Energy-dispersive X-ray spectroscopy (EDS) measurement were done with the Zeiss Auriga 60, using an EDAX Octane Super A detector controlled by EDAX TEAM software. EDS-mappings were carried out using 5 kV and 120 pA e-beam conditions and X-ray Lα-signals for Ga, Mz-signals for In and Sn.

**ADVANCED
SCIENCE NEWS**

www.advancedsciencenews.com

**ADVANCED
MATERIALS
TECHNOLOGIES**

www.advmattechnol.de

X-Ray Photoelectron Spectroscopy: The XPS measurements were done with a Thermofisher K-alpha system. Monochromatic Al-$k\alpha$ X-ray having photon energy 1480.6 eV. The emitted photoelectrons were collected to the analyzer at 90° to the surface of the sample. For depth profile sputtering monoatomic Ar+ ion with a kinetic energy of 500 eV was used. For data analysis, Thermofisher's Avantage software was used.

Encapsulation of Galinstan Interconnects with PMMA: The printed interconnects were encapsulated by spin coating with PMMA (from Micro Chem dissolved in Anisol) at 4000 rpm for 60 s with 10 s ramp up and ramp down times. The encapsulated interconnects were then placed on a hot plate at 150 °C for 3 min to cure the PMMA. After curing, the interconnects were again characterized by resistance measurements.

Gold Pad Printing: For the printing of gold pads, the glass capillary was filled with Au polymer ink from UT Dots, Inc. (UTDAu25-IJ) by dipping, utilizing the capillary force. Then, the ink was printed on the cleaned glass substrates (see substrate preparation) by contact spotting (bringing the capillary into direct contact with the substrate for a controlled time of 0.1 s). The substrates were then heated to 250 °C for 60 min for the Au polymer ink to become conductive.

Fully-Printed P–N Diode Fabrication: Based on the printed Au pad structures, fully printed p–n diode devices were constructed. The Galinstan bottom electrode was printed by glass capillary printing on the customized nanolithography system as described above (see Supporting Information). Then, In_2O_3 ink was printed with a Dimatix 2831 inkjet printer on top of the Galinstan bottom electrode and dried for 10 min at 100 ˚C. After this, the CuO ink was printed on top of the In_2O_3 pattern and dried as well for another 10 min at 100 °C. After drying, the substrate was annealed at 400 °C for 2 h to form the respective In_2O_3 and CuO phase. Finally, a conductive polymer (PEDOT: PSS) was printed on top of the p-type semiconductor film as the top electrode.

Fully-Printed FET Fabrication: For construction of a fully-printed FET device, again the printed Au pad structures were used as base. For the FET architecture, parallel Galinstan lines were printed with the glass capillary on the customized nanolithography system as described above. Then, the In_2O_3 precursor ink was applied with glass capillary between the Galinstan lines. After drying, the substrates were annealed at 400 °C for 2 h. Next, the CSPE ink was inkjet printed on top of the channel with a Dimatix 2831 inkjet printer, followed by the PEDOT:PSS as top-gate after the CSPE dried at RT. The devices were dried at 60 °C for an additional 30 min before measuring.

Optical Imaging Setups: Microscope imaging to trace length and widths of Galinstan interconnects as well as images for fully printed devices were performed using a Nikon Eclipse 80i upright microscope (Nikon, Japan) equipped with a Nikon DS-Qi2 camera (Nikon, Germany) and a broadband excitation light source (C-HGFIE Intensilight, Nikon). NIS-Elements imaging software was used to evaluate the devices measurements. Height measurements of printed interconnects/resistors were completed on a Veeco Dektak 6M Profilometer.

Atomic Force Microscopy: The atomic force microscopy (AFM) images were obtained on a Dimension Icon AFM (Bruker, Germany) in tapping mode under ambient conditions. The LM interconnects were scanned with AFM tips of a spring constant of 40 N m^{-1} and a nominal resonance frequency of 325 kHz (MikroMasch HQ:NSC15/Al BS AFM probe tips, MikroMasch, Wetzlar, Germany). AFM images were collected with NanoScope 9.7 software and processed with the freeware tool Gwyddion for the shown 3D image.

Electrical Resistivity Measurements: Resistance measurements of bare and encapsulated interconnect were conducted using an Agilent 4155C semiconductor parameter analyzer and a probe station with TRIAX probes with a current detection limit of 30 fA. Measurements were completed with voltage sweeps from −100 to +100 mV, and a step size of 5 µV; the average of 8 samples was used as a single data point.

P–N Diode and FET Characterization: The transistors and p–n diodes were characterized using Agilent 4156C semiconductor parameter analyzer and contacted through a probe station. The sweep rate was 10 mV s^{-1} in all cases.

Supporting Information

Supporting Information is available from the Wiley Online Library or from the author.

Conflict of Interest

G.M, U.B., J.A.H., and M.H. jointly hold a patent filed by KIT and published under WO2020039041A1 regarding the Galinstan writing process for fabrication of microelectronic devices.

Data Availability Statement

The data that support the findings of this study are available from the corresponding author upon reasonable request.

[1] M. D. Dickey, *Adv. Mater.* **2017**, *29*, 1606425.
[2] Y. Dai, H. Hu, M. Wang, J. Xu, S. Wang, *Nat. Electron.* **2021**, *4*, 17.
[3] P. Wang, M. Hu, H. Wang, Z. Chen, Y. Feng, J. Wang, W. Ling, Y. Huang, *Adv. Sci.* **2020**, *7*, 2001116.
[4] A. Tabatabai, A. Fassler, C. Usiak, C. Majidi, *Langmuir* **2013**, *29*, 6194.
[5] X. Wang, J. Liu, *Micromachines* **2016**, *7*, 206.
[6] Y. Gao, H. Ota, E. W. Schaler, K. Chen, A. Zhao, W. Gao, H. M. Fahad, Y. Leng, A. Zheng, F. Xiong, C. Zhang, L.-C. Tai, P. Zhao, R. S. Fearing, A. Javey, *Adv. Mater.* **2017**, *29*, 1701985.
[7] J. H. Oh, J. Y. Woo, S. Jo, C.-S. Han, *Sens. Actuators, A* **2019**, *299*, 111610.
[8] X. Zhou, R. Zhang, L. Li, L. Zhang, B. Liu, Z. Deng, L. Wang, L. Gui, *Lab Chip* **2019**, *19*, 807.
[9] K. Kim, J. Choi, Y. Jeong, I. Cho, M. Kim, S. Kim, Y. Oh, I. Park, *Adv. Healthcare Mater.* **2019**, *8*, 1900978.
[10] Y. R. Jeong, J. Kim, Z. Xie, Y. Xue, S. M. Won, G. Lee, S. W. Jin, S. Y. Hong, X. Feng, Y. Huang, J. A. Rogers, J. S. Ha, *NPG Asia Mater.* **2017**, *9*, e443.
[11] W. Zhang, J. Z. Ou, S.-Y. Tang, V. Sivan, D. D. Yao, K. Latham, K. Khoshmanesh, A. Mitchell, A. P. O'Mullane, K. Kalantar-zadeh, *Adv. Funct. Mater.* **2014**, *24*, 3799.
[12] H. Ota, K. Chen, Y. Lin, D. Kiriya, H. Shiraki, Z. Yu, T.-J. Ha, A. Javey, *Nat. Commun.* **2014**, *5*, 5032.

[13] M. G. Kim, H. Alrowais, C. Kim, P. Yeon, M. Ghovanloo, O. Brand, *Lab Chip* **2017**, *17*, 2323.

[14] S. Cheng, Z. Wu, *Lab Chip* **2010**, *10*, 3227.

[15] J. H. So, J. Thelen, A. Qusba, G. J. Hayes, G. Lazzi, M. D. Dickey, *Adv. Funct. Mater.* **2009**, *19*, 3632.

[16] M. Wang, C. Trlica, M. R. Khan, M. D. Dickey, J. J. Adams, *J. Appl. Phys.* **2015**, *117*, 194901.

[17] M. A. Rafi, B. D. Wiltshire, M. H. Zarifi, *IEEE Microw. Wirel. Compon. Lett.* **2020**, *30*, 469.

[18] R. S. Datta, N. Syed, A. Zavabeti, A. Jannat, M. Mohiuddin, M. Rokunuzzaman, B. Y. Zhang, M. A. Rahman, P. Atkin, K. A. Messalea, M. B. Ghasemian, E. D. Gaspera, S. Bhattacharyya, M. S. Fuhrer, S. P. Russo, C. F. McConville, D. Esrafilzadeh, K. Kalantar-Zadeh, T. Daeneke, *Nat. Electron.* **2020**, *3*, 51.

[19] Y. G. Park, H. S. An, J. Y. Kim, J. U. Park, *Sci. Adv.* **2019**, *5*, eaaw2844.

[20] J. Park, S. Wang, M. Li, C. Ahn, J. K. Hyun, D. S. Kim, D. K. Kim, J. A. Rogers, Y. Huang, S. Jeon, *Nat. Commun.* **2012**, *3*, 916.

[21] R. K. Kramer, C. Majidi, R. J. Wood, *Adv. Funct. Mater.* **2013**, *23*, 5292.

[22] L. Ren, J. Zhuang, G. Casillas, H. Feng, Y. Liu, X. Xu, Y. Liu, J. Chen, Y. Du, L. Jiang, S. X. Dou, *Adv. Funct. Mater.* **2016**, *26*, 8111.

[23] E. J. Markvicka, M. D. Bartlett, X. Huang, C. Majidi, *Nat. Mater.* **2018**, *17*, 618.

[24] J. Wissman, M. D. Dickey, C. Majidi, *Adv. Sci.* **2017**, *4*, 1700169.

[25] S. Y. Tang, K. Khoshmanesh, V. Sivan, P. Petersen, A. P. O'Mullane, D. Abbott, A. Mitchell, K. Kalantar-Zadeh, *Proc. Natl. Acad. Sci. U. S. A.* **2014**, *111*, 3304.

[26] I. A. De Castro, A. F. Chrimes, A. Zavabeti, K. J. Berean, B. J. Carey, J. Zhuang, Y. Du, S. X. Dou, K. Suzuki, R. A. Shanks, R. Nixon-Luke, G. Bryant, K. Khoshmanesh, K. Kalantar-Zadeh, T. Daeneke, *Nano Lett.* **2017**, *17*, 7831.

[27] S. Wang, L. Ding, X. Fan, W. Jiang, X. Gong, *Nano Energy* **2018**, *53*, 863.

[28] Y. Yang, J. Han, J. Huang, J. Sun, Z. L. Wang, S. Seo, Q. Sun, *Adv. Funct. Mater.* **2020**, *30*, 1909652.

[29] Y. Wu, L. Huang, X. Huang, X. Guo, D. Liu, D. Zheng, X. Zhang, R. Ren, D. Qu, J. Chen, *Energy Environ. Sci.* **2017**, *10*, 1854.

[30] S. A. Chechetka, Y. Yu, X. Zhen, M. Pramanik, K. Pu, E. Miyako, *Nat. Commun.* **2017**, *8*, 15432.

[31] M. Kim, D. K. Brown, O. Brand, *Nat. Commun.* **2020**, *11*, 1002.

[32] J. W. Boley, E. L. White, G. T. C. Chiu, R. K. Kramer, *Adv. Funct. Mater.* **2014**, *24*, 3501.

[33] Z. J. Farrell, C. Tabor, *Langmuir* **2018**, *34*, 234.

[34] F. Scharmann, G. Cherkashinin, V. Breternitz, C. Knedlik, G. Hartung, T. Weber, J. A. Schaefer, *Surf. Interface Anal.* **2004**, *36*, 981.

[35] L. Cademartiri, M. M. Thuo, C. A. Nijhuis, W. F. Reus, S. Tricard, J. R. Barber, R. N. S. Sodhi, P. Brodersen, C. Kim, R. C. Chiechi, G. M. Whitesides, *J. Phys. Chem. C* **2012**, *116*, 10848.

[36] N. Cho, S. Kang, H. Lee, H. Kang, G. D. Kong, H. J. Yoon, *Nano Lett.* **2021**, *21*, 360.

[37] T. Liu, P. Sen, C. J. Kim, *J. Microelectromech. Syst.* **2012**, *21*, 443.

[38] D. Kim, P. Thissen, G. Viner, D. W. Lee, W. Choi, Y. J. Chabal, J. B. Lee, *ACS Appl. Mater. Interfaces* **2013**, *5*, 179.

[39] V. Kocourek, *Elektromagnetisches Abstützen von Flüssigmetall-Tropfen*, Technische Universität Ilmenau, Ilmenau **2008**.

[40] S. Handschuh-Wang, Y. Chen, L. Zhu, X. Zhou, *ChemPhysChem* **2018**, *19*, 1584.

[41] C. Ladd, J. H. So, J. Muth, M. D. Dickey, *Adv. Mater.* **2013**, *25*, 5081.

[42] U. Bog, M. Hirtz, J. Aghassi, G. Cadilha Marques, S. Dasgupta, B. Breitung, H. Hahn, *WO2020039041A1*, **2020**.

[43] G. I. Livshits, J. Bao, L. Sakamoto, T. Misaka, Y. Usami, Y. Otsuka, T. Matsumoto, *Sci. Rep.* **2021**, *11*, 4670.

[44] Y.-G. Park, H. Min, H. Kim, A. Zhexembekova, C. Y. Lee, J.-U. Park, *Nano Lett.* **2019**, *19*, 4866.

[45] S. W. Jin, J. Park, S. Y. Hong, H. Park, Y. R. Jeong, J. Park, S.-S. Lee, J. S. Ha, *Sci. Rep.* **2015**, *5*, 11695.

[46] C. Surdu-Bob, S. Saied, J. Sullivan, *Appl. Surf. Sci.* **2001**, *183*, 126.

[47] N. Kornienko, J. Z. Zhang, K. K. Sakimoto, P. Yang, E. Reisner, *Nat. Nanotechnol.* **2018**, *13*, 890.

[48] E. R. Clifford, R. W. Bradley, L. T. Wey, J. M. Lawrence, X. Chen, C. J. Howe, J. Z. Zhang, *Chem. Sci.* **2021**, *12*, 3328.

[49] K. P. Sokol, D. Mersch, V. Hartmann, J. Z. Zhang, M. M. Nowaczyk, M. Rögner, A. Ruff, W. Schuhmann, N. Plumeré, E. Reisner, *Energy Environ. Sci.* **2016**, *9*, 3698.

[50] X. Lopez, K. Afrin, B. Nepal, *Med. Devices Sens.* **2020**, *3*, e10087.

[51] T. Ryynänen, M. Pekkanen-Mattila, D. Shah, J. Kreutzer, P. Kallio, J. Lekkala, K. Aalto-Setälä, *Jpn. J. Appl. Phys.* **2018**, *57*, 117001.

[52] R. Guo, J. Liu, *J. Micromech. Microeng.* **2017**, *27*, 104002.

[53] N. B. Morley, J. Burris, L. C. Cadwallader, M. D. Nornberg, *Rev. Sci. Instrum.* **2008**, *79*, 3.

[54] S. Cheng, Z. Wu, *Lab Chip* **2012**, *12*, 2782.

[55] G. Cadilha Marques, M. Tahoori, J. Aghassi-Hagmann, A. M. Sukuramsyah, A. Arnal Rus, S. Bolat, A. Aribia, X. Feng, S. A. Singaraju, E. Ramon, Y. Romanyuk, *IEEE Electron Device Lett.* **2020**, *41*, 187.

[56] G. C. Marques, S. K. Garlapati, D. Chatterjee, S. Dehm, S. Dasgupta, J. Aghassi, M. B. Tahoori, *IEEE Trans. Electron Devices* **2017**, *64*, 279.

[57] G. Cadilha Marques, S. K. Garlapati, S. Dehm, S. Dasgupta, H. Hahn, M. Tahoori, J. Aghassi-Hagmann, *Appl. Phys. Lett.* **2017**, *111*, 102103.

[58] X. Feng, C. Punckt, G. C. Marques, M. Hefenbrock, M. B. Tahoori, J. Aghassi-Hagmann, *IEEE Trans. Electron Devices* **2019**, *66*, 3365.

[59] T. T. Baby, G. C. Marques, F. Neuper, S. A. Singaraju, S. Garlapati, F. von Seggern, R. Kruk, S. Dasgupta, B. Sykora, B. Breitung, P. A. Sukkurji, U. Bog, R. Kumar, H. Fuchs, T. Reinheimer, M. Mikolajek, J. R. Binder, M. Hirtz, M. Ungerer, L. Koker, U. Gengenbach, N. Mishra, P. Gruber, M. Tahoori, J. A. Hagmann, H. von Seggern, H. Hahn, in *Functional Nanostructures and Sensors for CBRN Defence and Environmental Safety and Security* (Eds: A. Sidorenko, H. Hahn), Springer Nature B.V., Dordrecht **2020**, pp. 1–34.

[60] G. C. Marques, F. Von Seggern, S. Dehm, B. Breitung, H. Hahn, S. Dasgupta, M. B. Tahoori, J. Aghassi-Hagmann, *IEEE Trans. Electron Devices* **2019**, *66*, 2202.

[61] S. K. Garlapati, T. T. Baby, S. Dehm, M. Hammad, V. S. K. Chakravadhanula, R. Kruk, H. Hahn, S. Dasgupta, *Small* **2015**, *11*, 3591.